

A survey for variable young stars with small telescopes: II – mapping a protoplanetary disc with stable structures at 0.15 au

Jack J. Evitts,¹ Dirk Froebrich,^{1★} Aleks Scholz,² Jochen Eisloffel,³
Justyn Campbell-White[Ⓜ],^{1,4} Will Furnell,^{1,5} Bringfried Stecklum,³ Thomas Urtly,^{6†}
Roger Pickard,^{6†} Klaas Wiersema,^{7,8†} Pavol A. Dubovský,^{9†} Igor Kudzej,^{9†}
Ramon Naves,^{10†} Mario Morales Aimar,^{10,11†} Rafael Castillo García,^{10,11,12†}
Tonny Vanmunster,^{13,14†} Erik Schwendeman,^{11†} Francisco C. Soldán Alfaro,^{10,11†}
Stephen Johnstone,^{6,11†} Rafael Gonzalez Farfán,^{10†} Thomas Killestein,^{6,7†}
Jesús DelgadoCasal,^{10†} Faustino García de la Cuesta,^{10,15†} Dean Roberts,^{16†}
Ulrich Kolb,^{16†} Luís Montoro,^{10†} Domenico Licchelli,^{17†} Alex Escartin Perez,^{10†}
Carlos Perelló Perez,^{10,18†} Marc Deldem,^{11†} Stephen R.L. Fitcher,^{6,19†} Tim Nelson,^{19†}
Shawn Dvorak,^{11†} Dawid Moździerski,^{20†} Nick Quinn,^{6†} Krzysztof Kotysz,^{20†}
Katarzyna Kowalska,^{20†} Przemysław Mikołajczyk,^{20†} George Fleming,^{6†}
Mark Phillips,^{21†} Tony Vale,^{6,22,23†} Franky Dubois,^{24,25†} Ludwig Logie,^{24,25†}
Steve Rau,^{24,25†} Siegfried Vanaverbeke,^{24,25,26†} Barry Merrikin,^{19†}
Esteban Fernández Mañanes,^{10†} Emery Erdelyi,^{11,27†} Juan-Luis Gonzalez Carballo,^{10†}
Fernando Limon Martinez,^{10†} Timothy P. Long,^{28†} Adolfo San Segundo Delgado,^{10†}
José Luis Salto González,^{10,29†} Luis Tremosa Espasa,^{10†} Georg Piehler,^{30†}
James Crumpton,^{1‡} Samuel J. Billington,^{1‡} Emma D’Arcy,^{1‡} Sally V. Makin^{1‡}
and Lord Dover^{1‡}

Affiliations are listed at the end of the paper

Accepted 2020 January 15. Received 2020 January 15; in original form 2019 October 8

ABSTRACT

The HOYS citizen science project conducts long-term, multifilter, high-cadence monitoring of large YSO samples with a wide variety of professional and amateur telescopes. We present the analysis of the light curve of V1490 Cyg in the Pelican Nebula. We show that colour terms in the diverse photometric data can be calibrated out to achieve a median photometric accuracy of 0.02 mag in broad-band filters, allowing detailed investigations into a variety of variability amplitudes over time-scales from hours to several years. Using *Gaia* DR2, we estimate the distance to the Pelican Nebula to be 870^{+70}_{-55} pc. V1490 Cyg is a quasi-periodic dipper with a period of 31.447 ± 0.011 d. The obscuring dust has homogeneous properties, and grains larger than those typical in the ISM. Larger variability on short time-scales is observed in U and $R_c - H\alpha$, with U amplitudes reaching 3 mag on time-scales of hours, indicating that the source is accreting. The $H\alpha$ equivalent width and NIR/MIR colours place V1490 Cyg between CTTS/WTTS and transition disc objects. The material responsible for the dipping is located in a warped inner disc, about 0.15 au from the star. This mass reservoir can be filled and emptied

* E-mail: df@star.kent.ac.uk

† HOYS Observer.

‡ Observer Beacon Observatory.

on time-scales shorter than the period at a rate of up to $10^{-10} \text{ M}_{\odot} \text{ yr}^{-1}$, consistent with low levels of accretion in other T Tauri stars. Most likely, the warp at this separation from the star is induced by a protoplanet in the inner accretion disc. However, we cannot fully rule out the possibility of an AA Tau-like warp, or occultations by the Hill sphere around a forming planet.

Key words: stars: individual: V 1490 Cyg – stars: variables: T Tauri, Herbig Ae/Be – stars: formation, pre-main sequence.

1 INTRODUCTION

Young stellar objects (YSOs) were initially discovered by their irregular and large optical variability (Joy 1945). Their fluxes can be affected by a wide variety of physical processes such as changeable excess emission from accretion shocks, variable emission from the inner disc, and variable extinction along the line of sight (Carpenter, Hillenbrand & Skrutskie 2001). Furthermore, variability in YSOs occurs on a wide variety of time-scales – from short-term (minutes) accretion rate changes (e.g. Sacco et al. 2008; Matsakos et al. 2013) to long-term (years to tens of years) outburst or disc occultation events (e.g. Bozhinova et al. 2016; Contreras Peña, Naylor & Morrell 2019). Thus, observing variable young stars over a wide range of time-scales and wavelengths allows us to explore the physical processes, structure, and evolution of their environment, and provides key insights into the formation of stars.

Numerous photometric variability surveys have been conducted in the past aiming to address the study of YSO variability in optical and near-infrared filters. Often they have either focused on high cadence over relatively short periods [e.g. with COROT – Convection, Rotation, and planetary Transits – Auvergne et al. (2009), Kepler Cody et al. (2014), and Ansdell et al. (2016), and TESS – Transiting Exoplanet Survey Satellite, Ricker et al. (2015)] or longer term but lower cadence [e.g. with UKIRT Galactic Plane Survey – UGPS – and VISTA Variables in the Via Lactea – VVV – Contreras Peña et al. (2014); Contreras Peña et al. (2017)]. We have recently initiated the Hunting Outbursting Young Stars (HOYS) project that aims to perform high-cadence, long-term, and simultaneous multifilter optical monitoring of YSOs. The project uses a combination of professional, university, and amateur observatories (Froebrich et al. 2018b) in order to study accretion and extinction-related variability over the short and long terms in a number of nearby young clusters and star-forming regions.

Characterizing the structure and properties of the inner accretion discs of YSOs is vital for our understanding of the accretion processes and the formation of terrestrial (inner) planets in those systems. However, investigating the innermost disc structure of YSOs on scales below 1 au is currently only possible through indirect methods such as photometric monitoring of disc occultation events. Direct observations of discs with ALMA (Andrews et al. 2018) or SPHERE (Avenhaus et al. 2018) are limited to about 25–35 mas, which corresponds to 2.5–3.5 au for the nearest ($d \approx 100$ pc) young stars. Of particular interest are periodic or quasi-periodic occultation events [e.g. in AA Tau (Bouvier et al. 1999) or UX Ori-type objects (Herbst & Shevchenko 1999)] as they allow us to identify the exact physical location of the occulting structures in the discs based on the period, and thus to determine the spatial scales of the material directly.

In this paper, we aim to show how long-term optical photometric data from a variety of telescopes can be calibrated with sufficient accuracy to be useful for this purpose. With our light curves, we investigate the properties of the material causing quasi-periodic occultations in the young star V1490 Cyg. This paper is organized

as follows. In Section 2, we describe the HOYS data obtained for the project and detail the internal calibration procedure and accuracy for our inhomogeneous data set. We then describe the results obtained for V1490 Cyg in Section 3 and discuss the implications for the nature of the source in Section 4.

2 OBSERVATIONAL DATA AND PHOTOMETRIC CALIBRATION

2.1 The HOYS project

All data presented in this paper have been obtained as part of the HOYS project (Froebrich et al. 2018b). The project utilizes a network of amateur telescopes, several university observatories, and other professional telescopes, currently distributed over 10 different countries across Europe and the US. At the time of writing, the project had 58 participants submitting data, in several cases from multiple amateur observers or multiple telescopes/observing sites. In total, approximately 12500 images have been gathered. In those, we have obtained ≈ 95 million reliable photometric measurements for stars in all of the 22 HOYS target regions.

To ease and streamline the data submission and processing for all participants, we have developed an online portal. The website has been written using the DJANGO¹ web framework. DJANGO ORM has been used for managing the MariaDB data base² into which the processed data are automatically added. The website also allows users and the public to plot and download light curves³ for all objects in the data base.

2.2 V1490 Cyg imaging observations

In this paper, we analyse the data for the star V1490 Cyg, which is situated in the Pelican Nebula, or IC 5070, corresponding to the HOYS target number 118. At the time of writing, we have gathered a total of 85, 419, 1134, 932, 249, and 755 images in the U , B , V , R_c , $H\alpha$, and I_c filters, respectively, for this target field. The target itself has data with sufficient quality (magnitude uncertainty smaller than 0.2 mag) in 3321 images from 44 different users and 66 different imaging devices – see Section 2.3.2 for details. A full description of the observatories, the equipment used, the typical observing conditions and patterns, and data reduction procedures is given in Appendix A in the online supplementary material. All HOYS observations included in the paper for V1490 Cyg have been taken over the last 4 yr.

2.3 Photometric data calibration

The basic data calibration for all the HOYS data has been detailed in Froebrich et al. (2018b). The images are submitted to our

¹Django Project

²MariaDB

³HOYS Light curve Plotter

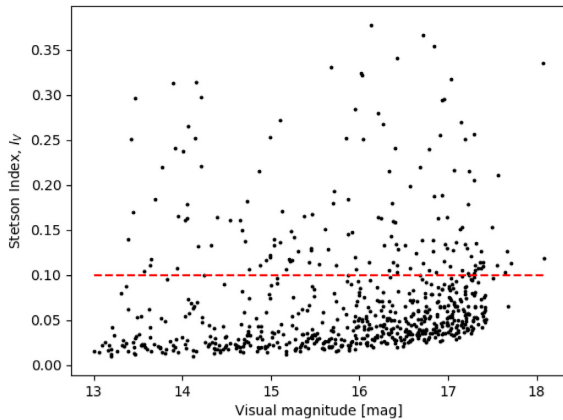


Figure 1. Stetson variability index \mathcal{I} against visual magnitude for all stars within the HOYS target region IC 5070. The red dashed line shows the cut made, below which stars were deemed to be non-variable.

data base server⁴ by the participants. They then indicate for each image which target region and imaging device (telescope/detector combination) have been used. We then extract the date/time, filter, and exposure time information from the FITS header and use the ASTROMETRY.NET⁵ software (Hogg et al. 2008) to accurately determine the image coordinate system.

2.3.1 Basic photometric calibration

The initial photometric calibration process is carried out on the data before it is submitted to the HOYS data base. The SOURCE EXTRACTOR⁶ software (Bertin & Arnouts 1996) is used to perform aperture photometry for all images. For each region and filter, a deep image obtained at photometric conditions has been chosen as a reference image. The U -band reference frames are from the Thüringer Landessternwarte (see Appendix A2.7 in the online supplementary material), while all the other reference images (B , V , R_c , I_c) are from the Beacon Observatory (see Appendix A2.5 in the online supplementary material). We have determined the calibration offsets into apparent magnitudes for those reference images by utilizing the Cambridge Photometric Calibration Server,⁷ which has been set up for *Gaia* follow-up photometry.

The magnitude-dependent calibration offsets $f(m_i)$ for all images into the reference frames have been obtained by fitting a photo-function and fourth-order polynomial $\mathcal{P}_4(m_i)$ (Moffat 1969; Bacher, Kimeswenger & Teutsch 2005) to matching stars with accurate photometry:

$$f(m_i) = A \log(10^{B(m_i - C)} + 1) + \mathcal{P}_4(m_i). \quad (1)$$

See section 2.4 in Froebrich et al. (2018b) for more details. Note that all $H\alpha$ images are calibrated against the R_c -band reference images. Typically, the accuracy of this basic relative calibration ranges from a few per cent for the brighter stars to 0.20 mag for the faintest detected stars, depending on the observatory, filter, exposure time, and observing conditions.

⁴HOYS Database Server

⁵Astrometry.net

⁶The source extractor

⁷Cambridge Photometric Calibration Server

2.3.2 Photometry colour correction

In Froebrich et al. (2018b), we limited the analysis to data taken either with the Beacon Observatory or data taken in the same filters. Now, with a much larger fraction of amateur data using a variety of slightly different filters, in particular from digital single-lens reflex (DSLR) cameras, the calibration of the photometry needs to consider colour terms. We have therefore devised a way to internally calibrate the photometry in the data base. The general steps of the correction process are outlined below.

The correction procedure utilizes stars in each target region that do not change their brightness over time. Hence, these stars do have a known magnitude and colour. By comparing the photometry (after the basic calibration described above) of these stars in an image to their known brightness, any difference can be attributed to colour terms caused by either the filter used, the sensitivity curve of the specific detector, or the observing conditions (e.g. thin/thick cirrus), which can then be corrected for. This will furthermore correct any systematic errors that have potentially been introduced during the basic calibration step. We thus need a reliable catalogue of non-variable stars for each HOYS target region.

2.3.3 Identifying non-variable stars

For each target region and in the V , R_c , and I_c filters, we identify the image with the largest number of accurately measured [SOURCE EXTRACTOR flag less than 5 – see Bertin & Arnouts (1996) for details] and calibrated magnitudes. Stars in those images that are detected in all three filters (matched within a 3" radius – the typical seeing in our images) are selected to generate a master list of stars for the region in our data base. For the selected stars, the accurately measured photometry in all filters (U , B , V , R_c , $H\alpha$, and I_c) is extracted. Stars with fewer than 100 data points in V , R_c , and I_c are removed. We then determine the Stetson index \mathcal{I} (Welch & Stetson 1993) for the V , R_c , and I_c data. Fig. 1 shows the Stetson index for V plotted against visual calibrated magnitude, for all stars within the target region of IC 5070. For the purpose of this paper, we classify stars with a Stetson index of less than 0.1 in all three filters (V , R_c , and I_c) as non-variable. For the non-variable stars, we determine the median magnitudes and colours in all of the filters (U , B , V , R_c , $H\alpha$, and I_c) as reference brightness for the subsequent calibration. The Stetson index cut ensures that images with small fields of view contain a sufficient number of calibration stars.

As can be seen in Fig. 1, there is a slight upward trend of the Stetson index in V for fainter stars, which is also seen in the R_c and I_c filters. This is caused by a small underestimation of the photometric uncertainties for the fainter stars during the basic photometric calibration due to images having different limiting magnitudes. The effect is, however, very small and thus has no significant impact on the selection of non-variable sources.

2.3.4 Colour correction

To correct for any systematic magnitude offset caused by colour terms, we determine for each image (N) a unique function $\mathcal{W}_N(m, c)$, where m is the calibrated magnitude of the stars in the image (in the filter the image is calibrated into) and c is the colour of the stars. For the purpose of this paper, we use $V - I_c$, but any other colour can be chosen if the star is detectable in those filters. The functional form of the correction factor used is a simple

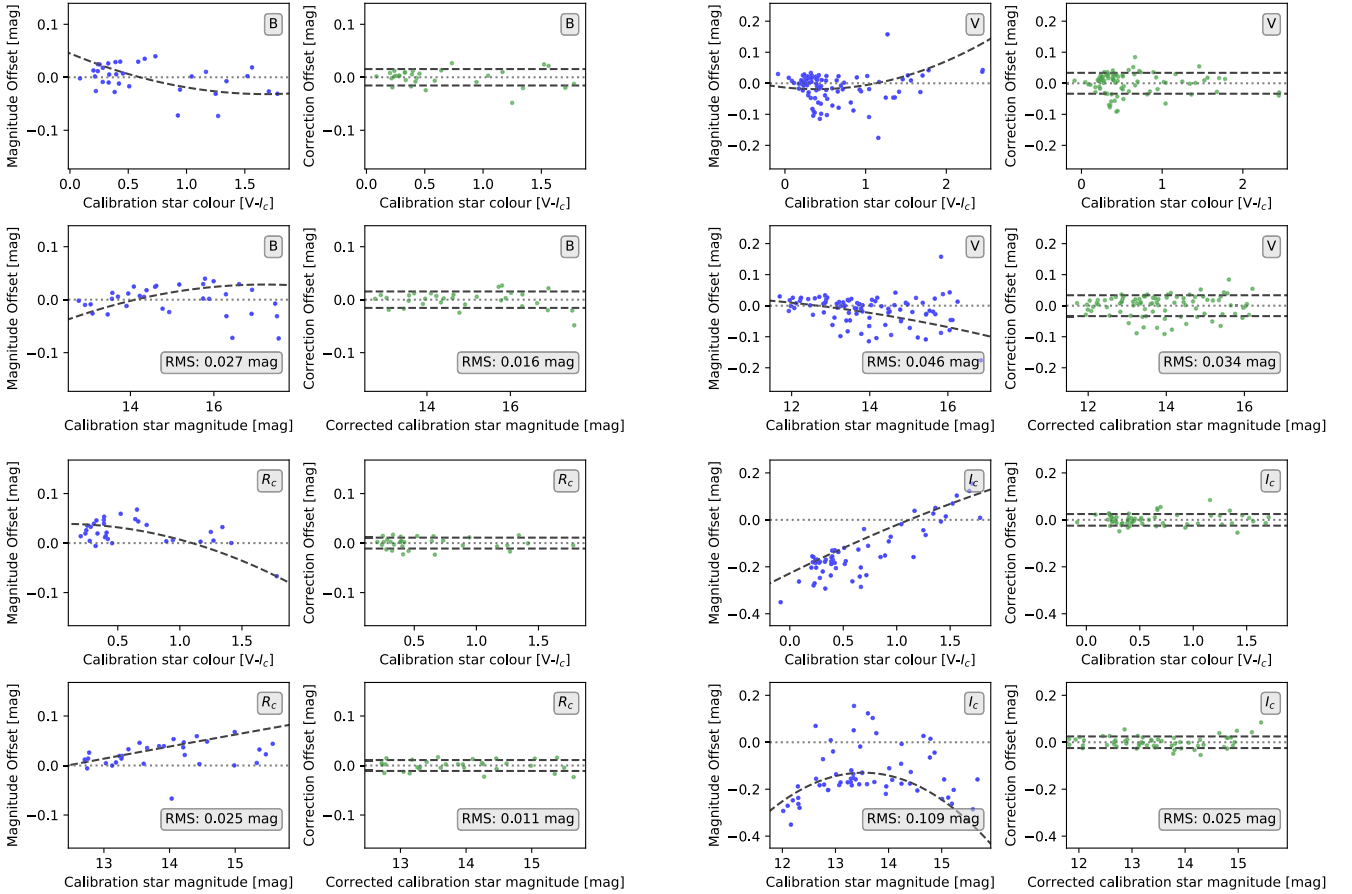


Figure 2. Example correction plots for four images in B , V , R_c , and I_c (from top left to bottom right). The B and V examples show very small colour terms, while the R_c and I_c images have been selected to show some of the largest colour terms present in our data to demonstrate how the colour correction procedure works. In each set of figures, there are four panels. **Top Left:** The dots show the offset calculated for each calibration star against their median colour ($V - I_c$). The dashed line shows $\mathcal{W}_N(m, V - I_c)$ for the median magnitude of the calibration stars. **Bottom left:** The dots show the offset calculated for each calibration star against their magnitudes. The dashed line shows $\mathcal{W}_N(m, V - I_c)$ for the median colour of the calibration stars. **Top right:** The dots show the corrected offsets for the calibration stars against their colour. **Bottom right:** The dots show the corrected offsets for the calibration stars against their magnitudes. All sigma-clipped stars are removed from the right-hand panels. The dashed lines in the right-hand panels indicate the RMS scatter after the correction.

second-order polynomial for both magnitude and colour, with no mixed terms and a common offset p_0 , i.e.

$$\mathcal{W}_N(m, V - I_c) = p_0 + \mathcal{P}^2(m) + \mathcal{P}^2(V - I_c), \quad (2)$$

where \mathcal{P}^2 represents a second-order polynomial without the offset. Thus, it is necessary to determine the five free parameters for the correction function $\mathcal{W}_N(m, c)$. We hence identify all non-variable stars detected (with SOURCE EXTRACTOR flag less than 5) in image N and determine their difference in magnitude from their real magnitude. We remove any stars that show a magnitude difference of more than ± 0.5 mag and whose magnitude uncertainty is greater than 0.2 mag. This is necessary, since stars selected as non-variable in V , R_c , and I_c may still change their brightness in U and $H\alpha$, especially if they are young and potentially accreting sources. We require at least 10 non-variable stars to be present in the image. We then perform a least-squares optimization of these magnitude differences to determine the required parameters for $\mathcal{W}_N(m, c)$. Typically, the bright non-variable stars in each image are far outnumbered by fainter ones, so for each star i , we introduce a magnitude m_i -dependent weighting factor w_i during the fitting

process:

$$w_i = \frac{1}{(m_i - \min(m_i) - 2)^2}. \quad (3)$$

Here, $\min(m_i)$ represents the magnitude of the brightest star included in the fitting process. This is the same weighting factor that is used when fitting the photofunction and fourth-order polynomial during the basic data calibration. This gives brighter stars a larger weight during the optimization. To ensure the fit is not influenced by misidentified objects, or stars showing variability (e.g. from flares not detected previously), the fitting is done using a 3σ clipping process. In Fig. 2, we show four examples of how the fitting process reliably removes any systematic colour- and magnitude-dependent photometry offsets.

To correct the magnitude m_i of a particular star i in image N using the determined parameters of $\mathcal{W}_N(m, V - I_c)$, the colour of the star must be known at the time of the observation for image N . We determine the median magnitude in V and I_c from all images taken within ± 5 d of the observation date to estimate the colour. If there are insufficient data, the time range is doubled until a value is found. As can be seen in Fig. 2, the colour dependence of the

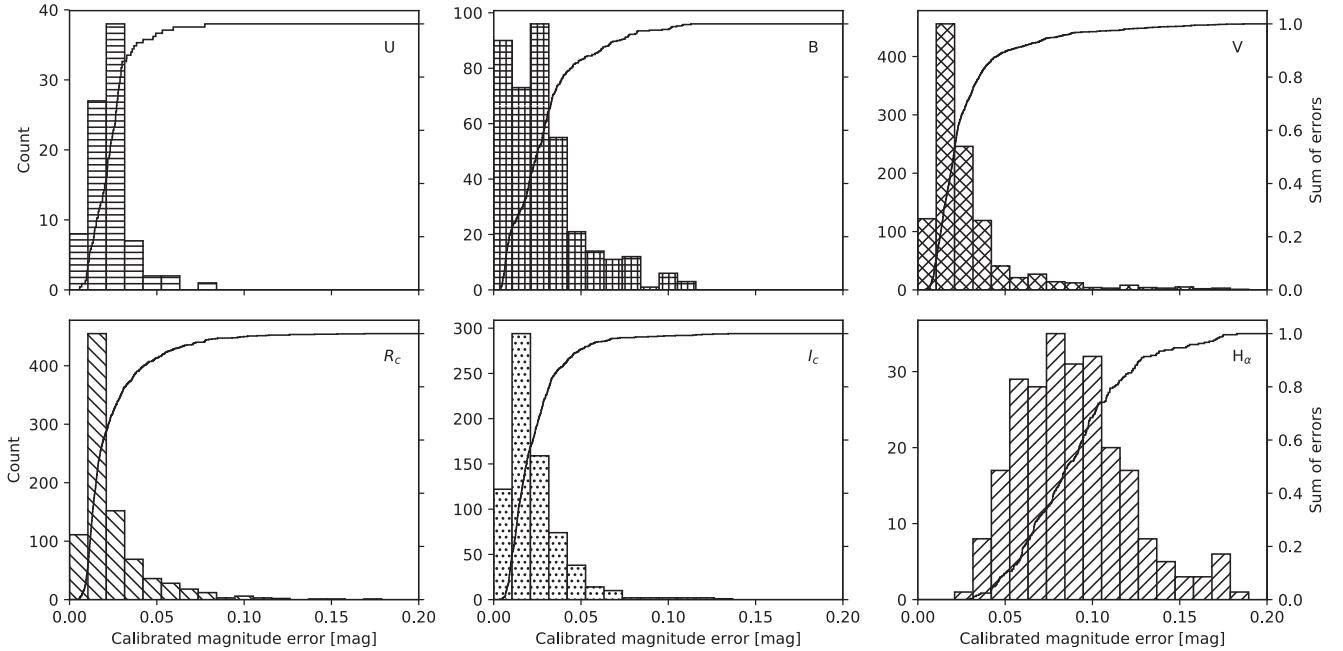


Figure 3. Histograms showing the number of the photometric uncertainties of all brightness measurements of V1490 Cyg after the colour correction. Each panel represents one of the filters. The solid line represents the cumulative distribution. One can see that more than 80 per cent of the V , R_c , and I_c measurements have photometric uncertainties of less than 0.04 mag.

correction is weak in all cases; thus, estimating the star’s colour from the uncorrected photometry will not introduce any considerable systematic offsets, particularly since the majority of the data have been obtained using filters that have a very small colour term.

We also use the calibration procedure to estimate a more representative uncertainty for the photometry after the correction of systematic offsets. We define the uncertainty as the RMS scatter of the magnitude offsets of all calibration stars in the image, which have the same magnitude (within ± 0.1 mag) as the star in question. If there are fewer than 10 calibration stars in that range, the magnitude range is increased until there are at least 10 calibration stars from which the RMS can be estimated.

The colour correction procedure only fails for 181 of the 3513 images when applied to the data of V1490 Cyg. The main reason for these failures is a very small field of view. The typical median calibrated magnitude uncertainties for the U and H_α filters are 0.08 and 0.09 mag, respectively. This decreases to about 0.02 mag for the B , V , R_c , and I_c filters. Fig. 3 shows histograms of all calibrated magnitude uncertainties that are less than 0.2 mag for each filter. The cumulative frequency distribution of the same data shows that approximately 80 per cent of the uncertainties in the broad-band filters are less than 0.04 mag.

The entire analysis presented in this paper has been conducted using the colour-corrected light curve for all data submitted and processed in the HOYS data base before 2019 September 1, and excludes any measurement with a higher than 0.2 mag photometric uncertainty after our colour correction procedure.

2.4 SPECTROSCOPIC DATA

From August 1 to September 15 in 2018, we coordinated HOYS observations in a high-cadence photometric monitoring campaign of V1490 Cyg in order to monitor the short-term variability of the source. In support of this campaign, we attempted to obtain

optical spectra of the source every 5 d. We utilized the FLOYDS spectrograph (Sand 2014) on the 2 m Las Cumbres Observatory Global Telescope network (LCOGT) telescope on Haleakala in Hawaii. It has a resolution between $R = 400$ (blue) and $R = 700$ (red) and covers a wavelength range from 320 to 1000 nm. Due to local weather conditions, observations were only carried out on six nights during the above-mentioned period. During each observing night, we took 3×600 s exposures of the target, using a slit width of $1.2''$.

We utilized the pipeline reduced spectra and downloaded them from the LCOGT archive. Spectra taken in the same night are averaged. The only feature visible in all the spectra is the H_α line. We therefore normalized the spectra to the continuum near the H_α line and determined the equivalent width (EW) of this line by fitting a Gaussian profile to it. We show the region around the H_α line for all spectra in Fig. 4.

3 RESULTS

3.1 The quasi-periodic light curve of V1490 Cyg

V1490 Cyg, also known as 2MASS J20505357+4421008, is located in the Pelican Nebula (IC 5070) at the J2000 position $RA = 20^h50^m53.58^s$, $DEC = +44^\circ21'00.88''$ (Gaia Collaboration 2018). It has been classified as a low-mass YSO and emission-line object by Ogura, Sugitani & Pickles (2002). The star is classified as a variable star of Orion Type (O_r^*) in the General Catalogue of Variable Stars (Samus et al. (2003)). It is not listed in Findeisen et al. (2013), who surveyed the area using data from the Palomar Transient Factory. It is included in the ASAS-SN variable stars data base⁸ (variable number 263219), but no period has been determined.

⁸<https://asas-sn.osu.edu/variables>

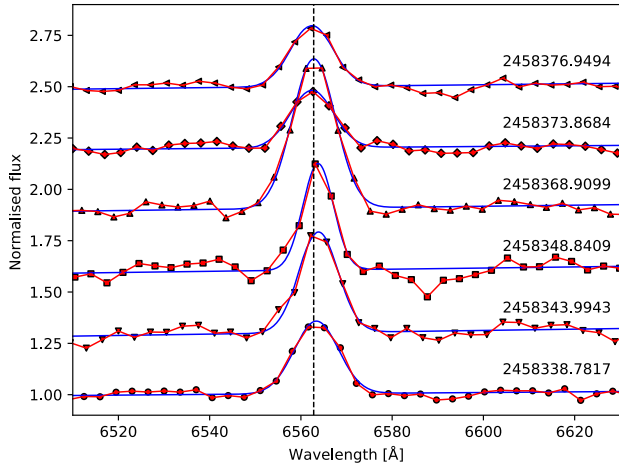


Figure 4. $H\alpha$ line profiles for V1490Cyg taken during 2018 August and September, ordered in time from bottom (earliest) to top (latest). The exact Julian dates are shown above each spectrum and the $H\alpha$ equivalent widths are listed in Table 3. The symbols and connecting red lines represent the data, while the smooth blue lines show the Gaussian fit to the $H\alpha$ line from which the equivalent widths are measured. The dashed vertical line indicates the nominal $H\alpha$ wavelength.

Table 1. Ranges of variability for each filter for V1490Cyg. Given are the minimum recorded magnitudes, the maximum recorded magnitudes, and the difference between them.

Filter	min (mag)	max (mag)	Δm (mag)
U	18.18	14.92	3.26
B	18.70	16.60	2.10
V	17.31	15.03	2.27
R_c	15.96	13.97	1.99
$H\alpha$	15.29	11.00	4.29
I_c	15.26	13.65	1.61

V1490Cyg was, however, included in the list of candidates for YSOs published by Guieu et al. (2009) and has been further studied by Ibryamov et al. (2018), who do not report any periodicity. Froebrich et al. (2018a) investigate the source and determine a period of approximately 31.8 d in the V band. In the analysis of HOYS data by Froebrich et al. (2018b), it was classified as one of the most variable sources, grouped into the extreme dipper category. The colour and brightness changes were estimated to be caused by extinction due to dust grains that are larger than typical ISM grains.

The 4 yr long-term HOYS light curves of V1490Cyg, observed between 2015 September and 2019 September in the U , B , V , R_c , $H\alpha$, and I_c filters, are shown in Figs. B1, B2, and B3 in Appendix B in the online supplementary material. The object shows strong variability, with large amplitude changes ($\Delta m > 1$ mag) in all filters, in agreement with its classification as a variable star by Samus et al. (2003). In Table 1, we list the range of maximum variability in each filter. The brightness variations of V1490Cyg are seen over the entirety of our observing period.

In Fig. 5, we show a close-up of the light curve in U , B , V , R_c , and I_c , as well as for $R_c - H\alpha$ for the time period from 2018 August 1 to September 15, where we ran a focused coordinated campaign with all participants in order to investigate the short-term variability of the source. This figure clearly shows distinct, short-duration changes (down to sub-one day) in the brightness of the source during this 45 d observing period. In the four broad-band filters (B , V , R_c , and

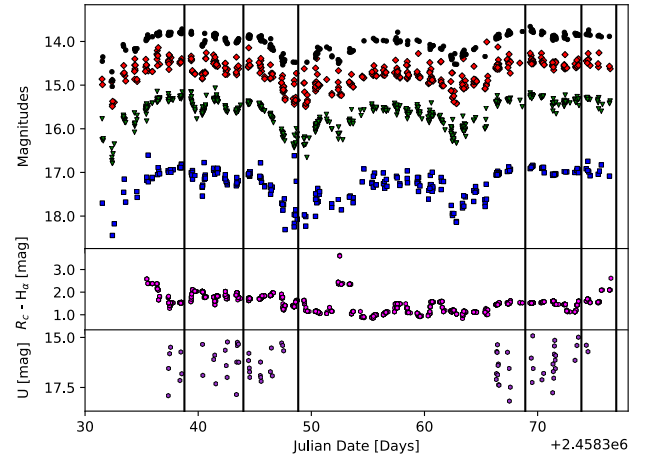


Figure 5. Top panel: HOYS light curves in B (blue), V (green), R_c (red), and I_c (black) of V1490Cyg for the high-cadence campaign run between 2018 August 1 and September 15. Middle panel: $R_c - H\alpha$ magnitudes for V1490Cyg for the same time period. Bottom panel: U magnitudes for V1490Cyg for the same time period. The vertical lines in all the panels indicate the times when the LCOGT spectra are taken.

I_c) the light curves look very similar, i.e. they show exactly the same behaviour and only the amplitudes are different. The U -band data, even if much more sparse, do not follow this trend and show variability with $\Delta U \sim 3$ mag. We will discuss this in more detail in Section 3.2. The $R_c - H\alpha$ light curve also does not follow the general trend of the broad-band filters, but it shows longer term (weeks) and short-term (day/s) variability with short, up to 1 mag bursts.

A more detailed investigation of the entire 4 yr light curve reveals that the variations in the star’s brightness occur as dips in brightness lasting from a few days to about two weeks. We used Lomb–Scargle periodograms (Scargle 1982) to investigate whether or not these dips are periodic in nature. The periodograms for the B , V , R_c , and I_c filters are shown in Figs. C1 and C2 in Appendix C in the online supplementary material. We can identify that V1490Cyg exhibits a clear quasi-periodic behaviour for the broad-band filters V , R_c , and I_c , with a period of approximately 31.5 d, in agreement with Froebrich et al. (2018a).

Utilizing the V , R_c , and I_c HOYS data, we find an average period of the dips of 31.423 ± 0.023 d. The uncertainty is the RMS of the periods determined for the individual filters. In order to improve the accuracy, we include the V , R_c , and I_c data from Ibryamov et al. (2018) in our period determinations as this extends the observation period from 2010 September to 2019 September, i.e. doubling the baseline of the data. We have ‘colour corrected’ the Ibryamov et al. (2018) data using common observing dates between their and our data. The mean period with the additional data for the three filters then becomes 31.447 ± 0.011 d, which we will use for the purpose of this paper throughout. The phase zero-point (taken to be the point of maximum light) occurs at $JD = 2458714.0$, which corresponds to 12:00 UT on 2019 August 18. The phased light curves in Figs. C1 and C2 in the online supplementary material indicate that the object is most likely to be observable in its bright state within about ± 5 d (15 per cent of the period) from the nominal phase = 0 point.

Note that despite the much smaller amount of B -band data in our light curve, the periodogram shows a peak at the above-determined period (see Fig. C1 in the online supplementary material). The peak is, however, not as significant as for the other filters.

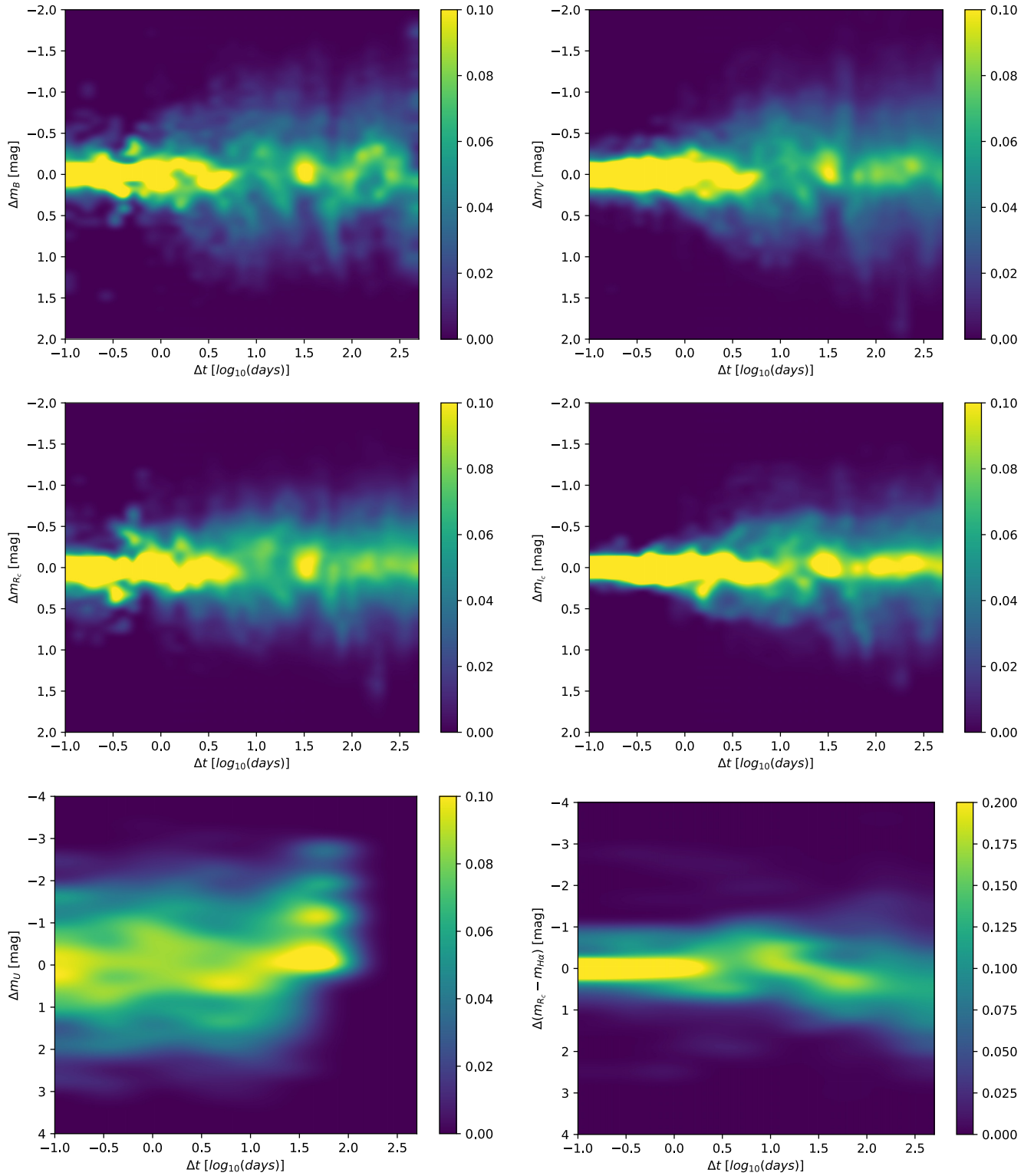


Figure 6. Variability fingerprint plots of B , V , R_c , I_c , U , and $R_c - H\alpha$ data (top left to bottom right) for V1490 Cyg. The colours indicate the probability of observing the object to undergo a change in magnitude for a given time gap between observations. Clearly observed in the B , V , R_c , and I_c fingerprints is the periodicity of V1490 Cyg at $\log(\Delta t) \approx 1.5$, which equates to the determined period of 31.447 d. The bin size in the top four plots is 0.08 mag and a factor of 1.237 for Δt , and in the bottom two plots the bin size is 0.27 mag and a factor of 2 for Δt .

3.2 Analysis of the variability fingerprints

In order to further analyse the star's variability, in particular to investigate time-scales and amplitudes, we determine a *variability fingerprint* of the source in each filter. This follows and improves upon previous work by, e.g. Scholz & Eislöffel (2004), Findeisen, Cody & Hillenbrand (2015), and Rigon et al. (2017). We determine, for all data points in a light curve that are taken in the same filter, all possible time (t) and magnitude (m) differences for two measurements i, k ($\Delta t = t_i - t_k$; $\Delta m = m_i - m_k$), where $t_i > t_k$. All these differences are then used to populate a 2D Δt versus Δm histogram, where the bins in Δt are log10 spaced. These histograms are normalized to an integral of one for each bin of Δt . This ensures that the values in these variability fingerprints represent the probability (p) that the source shows a change of Δm for a given time interval Δt between observations.

In Fig. 6, we show these variability fingerprints for V1490 Cyg for the five broad-band filters as well as for $R_c - H\alpha$. The plots for B , V , R_c , and I_c (top four plots) show an extremely similar behaviour; however, the B -band data suffer from a smaller number of observations compared to the other filters. For time intervals between observations shorter than a few days, the object is most likely not variable and is observed at the same magnitude. The width of the high-probability ($p > 10$ per cent) behaviour corresponds very well to the typical photometric errors measured in the photometry of the object after the calibration procedure (see Fig. 3 in Section 2.3.2).

Between 10 and 30 d intervals, the probability to find the object changed within its range of variability is almost homogeneously distributed. At a roughly 30 d interval, the object is once again most likely to be observed at an unchanged magnitude, representing the quasi-periodicity of the source. However, there is still a significant probability that the source does not return to precisely the same brightness after one period. This indicates that the internal structure of the dips varies each time it is observed. We will investigate this in more detail in Section 3.3.

For time intervals longer than 30 d, the fingerprints show that the object most likely does not change brightness but still has a significant probability to show variations within the min/max values found for each filter. Thus, the overall behaviour of the object remains unchanged for time-scales beyond one period. Furthermore, one can see that from time intervals of 1 d onward, there is a non-zero probability that the object starts to vary by more than the photometric uncertainty. In the Δt versus Δm space, this trend is almost linear from 1 d to about half the period, after which the variability does not increase any further. This short-term variability is also very evident in the detailed light curve presented in Fig. 5.

Compared to the B , V , R_c , and I_c fingerprints, the behaviour for U and $R_c - H\alpha$ is different (see the bottom graphs in Fig. 6). This difference is not just caused by the reduced number of observations available and the (particularly in the U band) much shorter total time interval covered by the observations.

In the U band, the variability for short time intervals is clearly different from the photometric uncertainties and also does not systematically increase towards one period. In essence for U the full range of variability is achieved within time intervals of less than 1 d. Furthermore, the magnitude of variability is much larger. For example, the U -band magnitude changes by up to 3 mag in a single night. Variability in the U -band fluxes is indicative of accretion rate changes (Calvet & Gullbring 1998; Gullbring et al. 1998; Herczeg & Hillenbrand 2008). This indicates short-term (hours) accretion rate fluctuations in this object by a factor of up to 10 or slightly larger. This will be discussed in more detail in Section 4.4.

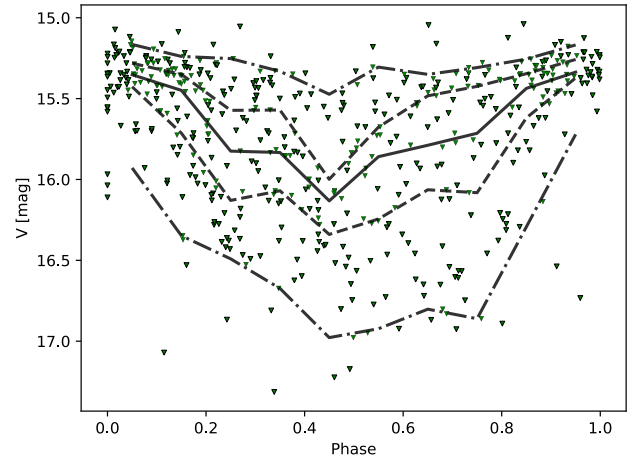


Figure 7. Phased light curve of V-band data for V1490 Cyg. The solid line indicates the running median magnitude. The two most extreme dash-dotted lines indicate the range within which 95 per cent of the data points can be found. The other two dashed lines indicate the 68 per cent range for the data points. Note that the high-cadence data (shown in Fig. 5) have been removed from this plot as it otherwise would dominate the typical shape due to the large amount of data in that 6 week period.

The $R_c - H\alpha$ fingerprint over short time periods (i.e. less than a few days) is similar to the B , V , R_c , and I_c filters, in that it is dominated by the photometric uncertainties, which are of course higher for the $H\alpha$ images. However, there is a non-negligible probability that the source varies by up to 1 mag even at those short time intervals. This is caused by short bursts of variability, one of which is evident in the detailed light curve in Fig. 5. However, there is no strong indication that the $R_c - H\alpha$ magnitude follows the same periodic behaviour that can be seen in the broad-band filters. Generally, the variability in $R_c - H\alpha$ increases slightly with an increase in time interval between observations. The apparent trend of a slight long-term decrease in $R_c - H\alpha$ visible in the fingerprint plot is not real, as it depends upon a single $H\alpha$ data point.

3.3 Column density distribution of consecutive dips

The quasi-periodic dips in the light curve of V1490 Cyg are potentially caused by orbiting material in the accretion disc. The different time-scales of the variability in the U and $H\alpha$ filters strongly suggest that accretion variability is not the cause of the longer term variations in the B , V , R_c , and I_c continuum. In the following, we aim to constrain the properties of the occulting material.

The quasi-periodic nature of V1490 Cyg found in Section 3.1 indicates orbiting material held in place within the inner disc for at least the duration of our light curve, i.e. more than 4 yr. As evident in the variability fingerprint plots shown in Fig. 6, there is a significant probability that the source does not return to the exact same brightness after one full period. This indicates variation in the column density distribution of the material along its orbital path. In this section, we will investigate if we can identify any systematic changes in the column density distribution, which can hint at the time-scales and/or mechanisms by which the material is either moved into and out of the orbiting structure, or redistributed within it.

In Fig. 7, we show the folded V-band light curve of V1490 Cyg with the high-cadence data from 2018 August to September (shown in Fig. 5) removed as this would otherwise dominate the analysis.

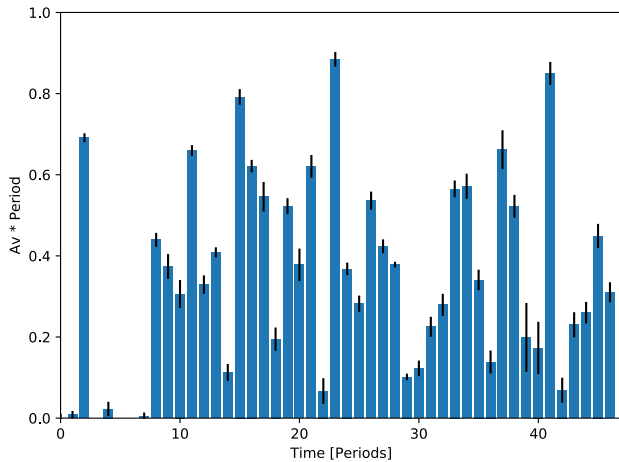


Figure 8. This plot shows the integrated column density for each orbital period, i.e. a measure of the mass of material contained in the orbiting structure around V1490 Cyg for the observed dips. The dips are numbered arbitrarily starting at our first available data. The value of one on the y-axis corresponds to about $1 \times 10^{-11} M_{\odot}$ or 0.03 per cent of the Lunar mass.

The plot has the running median overlaid, which indicates the typical column density distribution of material along the orbit. As one can see, the median occultations are up to about 0.7 mag deep and have a broad minimum. In the figure, we also show the typical 1σ and 2σ deviations from the median, which are represented by the dashed and dash-dotted lines, respectively. They indicate that in some cases there is almost no detectable occultation, while the dips can, in extreme cases, be up to 1.7 mag deep in the V band, during a larger part of the period.

Our HOYS data now cover about 40 complete periods of V1490 Cyg. We are hence able to investigate how the column density distribution along the orbital path varies as a function of the time interval between observations (in units of the period of the source). In essence, we can construct the structure function of the column density. For this, we determine the difference $\Delta(m)$ in the depth of the dip for all pairs of V-band measurements, which are N times the period (± 1 d) apart from each other, whereby N runs from 1 to 10. We find that there are no significant trends in the structure function and hence refrain from showing it here. The values for $\Delta(m)$ scatter less (for all values of N) when the phase is close to 0 or 1, compared to phase values near 0.5. This is of course expected from Fig. 7. There are no systematic trends for the value of the structure function with N , either for a particular part of the phase space, or when averaged over the entire period.

Given the lack of correlation found above of column density from dip to dip, we have tried to investigate the total amount of material along the orbital path during each dip. Under the assumption of a constant line of sight column density, the mass is proportional to the integrated depth of the V-band light curve for each dip. We show the results of this calculation in Fig. 8. We use a trapezium interpolation between V-band data points to determine the values displayed in the figure. The error bars are solely based on the photometric uncertainty and do not consider gaps in the data. As one can see, the amount of mass in the occulting structure varies by up to a factor of 10. This suggests that the material in the line of sight is moving in and out of the structure on time-scales of the order of, or shorter than the period of the occultations, and the mass flow rate varies by typically a factor of a few when averaged over one period. This is in agreement with the R_c – $H\alpha$ and U-band variability

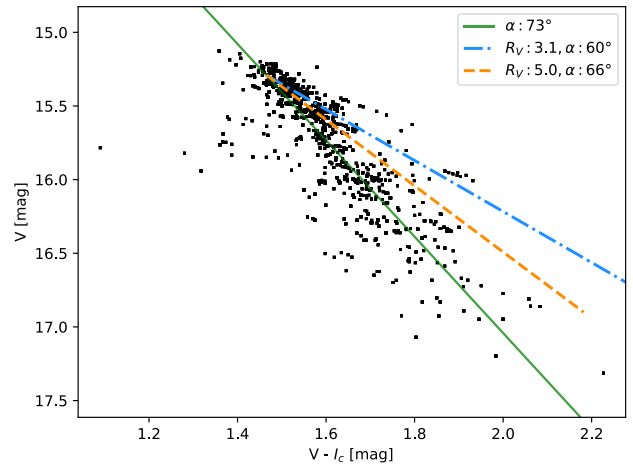


Figure 9. The V versus $V-I_c$ colour magnitude plot for the HOYS data of V1490 Cyg. The blue dash-dotted line corresponds to behaviour expected for occultations by material with $R_V = 3.1$, while the orange dashed line is for $R_V = 5.0$. The solid green line indicates the determined angle for V1490 Cyg of 73° .

discussed in the previous sections, which indicate variable accretion through the disc.

We can make some simple assumptions about the star and the geometry of the occulting structure to obtain an order of magnitude estimate of the mass in the dips. Given the classification of the source as low-mass YSOs (Ogura et al. 2002), we assume that the object has a central mass of $0.5 M_{\odot}$. The period of about 31.5 d then means that the occulting material is located about 0.15 au from the central star. We further assume dimensions of the structure in the two directions perpendicular to the orbital path of 0.05 au, and dust scattering properties in agreement with $R_V = 5.0$ (see below in Section 3.4). This converts the value of one in Fig. 8 to approximately $1 \times 10^{-11} M_{\odot}$ (or 0.03 per cent of the Lunar mass). Given the period, the typical mass flow (accretion rate) of material through the structure in V1490 Cyg is hence of the order of $10^{-10} M_{\odot} \text{ yr}^{-1}$. This is consistent with low levels of accretion as seen in other T Tauri stars (e.g. Alcalá et al. 2017).

3.4 Colour variations during dips

In order to investigate the scattering properties of the occulting material in the line of sight during the dips, we investigate the star's behaviour in the V versus $V-I_c$ parameter space.

To characterize the movement of the star in this diagram, we follow Froebrich et al. (2018b) and determine the angle α , measured counterclockwise from the horizontal. Using a standard reddening law by, e.g. Mathis (1990), disc material composed of normal ISM dust would have α values between 60° ($R_V = 3.1$) and 66° ($R_V = 5.0$). We show the V versus $V-I_c$ diagram for V1490 Cyg in Fig. 9. Note that the exact values for α do also depend on the filter transmission curves used in the observations. However, there will be a general trend of increasing α values with increasing typical grain size. Occultations by very large grains compared to the observed wavelengths, or by optically thick material, should generate colour-independent dimming ($\alpha = 90^\circ$). If occultations cause a change in the dominant source of the light we observe, i.e. from direct light to scattered light, other colour changes including bluing during deep dimming events can occur; see e.g. Herbst & Shevchenko (1999).

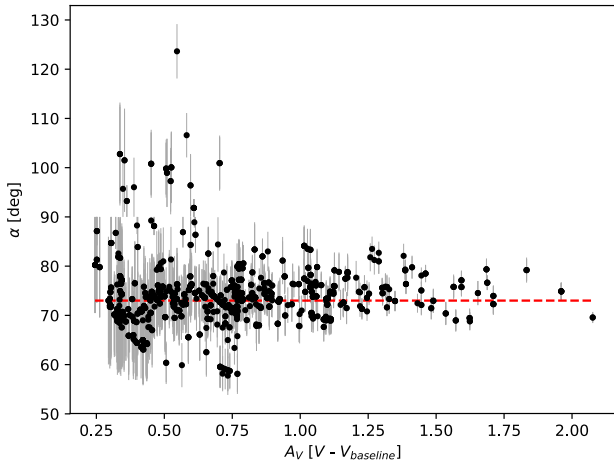


Figure 10. α values in the V versus $V-I_c$ parameter space during dips as a function of dip depth, i.e. A_V . Points were removed within 5σ of the V -band baseline of 15.29 mag. The red dashed line indicates the median α value of $(73 \pm 4)^\circ$.

Since the determined value of α can be very sensitive to small changes in the V and $V-I_c$ values, we only include high-signal-to-noise (S/N) measurements in this analysis. In particular, we only include V and I_c magnitudes that have a determined uncertainty of less than 0.05 mag after the colour correction (see Section 2.3.2). Furthermore, since the object is constantly changing its brightness the V and I_c data need to be taken as simultaneously as possible. Thus, we only utilize pairs of V and I_c data that were obtained within 1 d.

In order to determine α , we need to establish the baseline brightness in V and I_c , which represents the bright state of the source. We select all data that are taken at a phase within 0.1 from the bright state of the source (see Section 3.1) and use their median magnitude as the baseline brightness for the source. This equates to 15.29 mag in V and 13.86 mag in I_c . The uncertainty in α is determined from error propagation of the individual photometry errors obtained during the colour correction.

In Fig. 10, we show the α values plotted against the depth of the occultation in the V band, i.e. the A_V of the occulting material. We only include points that correspond to measurements taken at an occultation depth of more than 5 times the nominal maximum uncertainty of the V -band data, i.e. when the dip is deeper than 0.25 mag. The median value for α is 73° with a scatter of 4° . This angle is systematically higher than what can be expected for normal interstellar dust-grain-dominated scattering. Hence, the disc material in V1490 Cyg does show signs of the onset of general grain growth in the higher column density material.

There is no significant systematic trend of α with A_V , i.e. the occulting material has the same scattering properties (within the measurement uncertainties) independent of the column density of the material or time, for an extinction above 0.25 mag in V . There are a few outlying points that are significantly further away from the other data. These points occur at ‘random’ places in the light curve and thus are not caused by single, or multiple dip events with material with different scattering properties. Hence, the outliers are most likely caused by erroneous data where the initial magnitudes have been influenced by, e.g. cosmic ray hits, or where the up to 1 d time gap between the V and I_c observations causes unrealistic values for α . As one can see in Fig. 5, significant brightness variations in the source can occasionally happen on time-scales of less than 1 d.

As noted above, small uncertainties in the V and I_c magnitudes can lead to large uncertainties in the α value. The $V-I_c$ colour is used in the calibration of the magnitudes (see Section 2.3.2). Thus, if initially not exactly correct, the calibration will give systematically different magnitudes and hence might cause systematic and/or random offsets in α . As evident from the light curves and Fig. 9, the $V-I_c$ colour of the source varies by a maximum of about 0.5 mag between the bright and faint state. To test the influence on the determination of α , we have run the following experiment. We have rerun the entire calibration procedure with a systematically overestimated $V-I_c$ colour by 0.5 mag (the worst case scenario). This, of course, has a systematic effect on the newly calibrated magnitudes of the star. Note that the colour dependence of the calibration is, however, rather weak (see Fig. 2). We have then redetermined all the α values and compared them to the original numbers. We find that there are no significant changes to the scatter and uncertainties for α other than a systematic shift by 1° (to 72°) of the median value. Thus, our results for the scattering properties are robust, and the α values do not suffer any systematic uncertainties bigger than 1° caused by the calibration procedure.

A detailed look at Fig. 9 reveals that for dip depths of less than 0.25 mag in V , the scattering behaviour of the material does not follow the same slope as determined for the high A_V material. We performed a linear regression of all low extinction points and found that in the V versus $V-I_c$ diagram they are consistent with $R_V = 5.0$ scattering material. Thus, this suggests that the material in the occulting structure consists of low-column density material with roughly ISM dust properties. Embedded in this envelope are denser, small-scale structures that are most likely composed of larger dust grains. The scattering properties of this material are consistent and do not change over time.

4 DISCUSSION

4.1 Distance of V1490 Cyg

As V1490 Cyg is projected on to IC 5070, it is assumed to be part of this large star-forming region, whose distance was estimated to be about 600 pc (Reipurth & Schneider 2008; Guieu et al. 2009). With the availability of *Gaia* DR2, we can re-evaluate the distance of the source. V1490 Cyg is identified as *Gaia* DR2 2163139770169674112 with $G_{\text{mag}} = 15.0771$ mag, a proper motion of -0.539 ± 0.377 mas yr $^{-1}$ in RA and -2.418 ± 0.370 mas yr $^{-1}$ in DEC, and a parallax of 0.4560 ± 0.2377 mas. This indicates a much larger distance of 2.2 kpc with a very high uncertainty.

In order to verify the distance, we downloaded all *Gaia* DR2 sources within $20'$ of the object. If one selects only stars with an S/N of three or higher for the parallax, then the IC 5070 region stands out as a cluster in proper motion versus parallax plots (see Fig. D1 in Appendix D in the online supplementary material). The cluster is not identifiable in proper motion space alone, but IC 5070 members have proper motions in the range from -0.35 to -2.00 mas yr $^{-1}$ in RA and from -2.00 to -5.00 mas yr $^{-1}$ in DEC. The cluster overdensity seems to extend from parallaxes of 1.0 to 1.5 mas. A Gaussian fit to the parallax distribution (including only objects with an S/N better than 10 for the parallax) gives a mean parallax of ≈ 1.2 mas with a standard deviation of 0.09 mas (see Fig. 11). If we apply the suggested zero-point correction of -0.0523 mas (Leung & Bovy 2019), this indicates a distance for IC 5070 of the order of 870^{+70}_{-55} pc, which we will adopt throughout this paper for this region and V1490 Cyg.

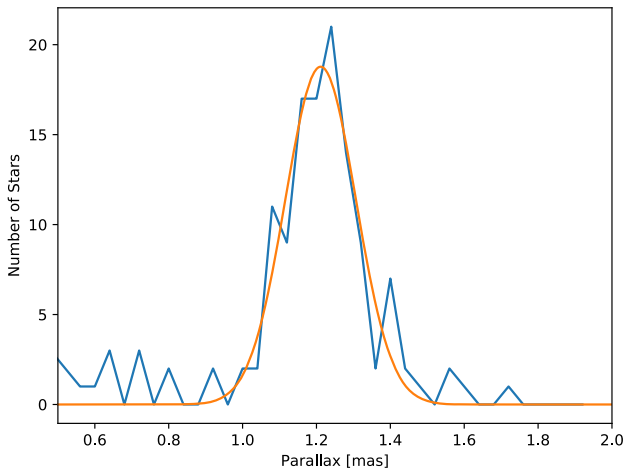


Figure 11. Distribution of *Gaia* DR2 parallaxes in the IC 5070 region with a parallax S/N of better than 10 and proper motions corresponding to IC 5070 member stars. Overplotted is a Gaussian fit to the data, indicating a mean parallax of 1.20 mas with a scatter of 0.09 mas.

To understand why the parallax of V1490 Cyg differs from the cluster value and also has a very low S/N ratio, we determine the typical parallax error of all stars in the same field, with proper motions indicating that they are potentially part of IC 5070 and with a Gmag value within 1 mag of V1490 Cyg – there are 49 such stars. For those stars, the median parallax error is $0.046 \text{ mas yr}^{-1}$ with a scatter of $0.021 \text{ mas yr}^{-1}$. Hence the parallax error of $0.2377 \text{ mas yr}^{-1}$ represents an $\approx 9\sigma$ outlier. The source does not stand out in terms of the number of observations when compared to stars in the same field; thus, there is no general issue with crowding in this field. However, the astrometric excess noise is much higher for this object, as well as all other quality indicators. This indicates that the object’s parallax measurements could be influenced by: (i) crowding for this source, caused by the scan angles used so far; (ii) the red colour and variability; (iii) the source being a binary or that the object’s photocentre position changes due to the variability. Thus, the *Gaia* DR2 parallax of the source cannot be trusted and we use the above-determined IC 5070 distance. We will briefly discuss the binary interpretation in Section 4.2. There is of course a possibility that the source is indeed a background object.

4.2 Potential binarity of V1490 Cyg

The large *Gaia* parallax error indicates that the star could be a binary, unresolved in our optical images. We have investigated the highest resolution imaging data available of this source, which comes from the UKIDSS GPS survey (UGPS; Lucas et al. 2008). The NIR images reveal three faint, red NIR objects around the star, at separations of 5.6, 2.7, and $2.5''$. However, they are fainter by 2.5, 4.5, and 7.0 mag in *K*, and fainter in *J* by 3.6 and 5.6 mag – the closest source has no *J* detection. V1490 Cyg itself has the maximum possible value of $p_{\text{star}} = +0.999999$, indicating that its PSF is consistent with a single unresolved source. The ellipticities in all three filters are between 0.07 and 0.10, indicating that the source is not elongated at a level above 0.1 of the full width at half-maximum of the PSF. The seeing in the images is about $0.56''$. Thus, any companion not detectable in UGPS would have to be closer than $0.05''$ to the source. At our adopted distance of 870 pc, this corresponds to about 44 au maximum separation.

However, the periodic variability of the source is not in agreement with a wide (30–40 au) binary with comparable luminosities. The period of about 31.5 d indicates material at sub-au distance from the star. The depth of some occultations reaches up to 2 mag in *V*. For equal luminosity objects with one partner being occulted, one should not obtain such deep dips. The maximum dip should only be 0.75 mag. If the stars are unequal luminosity then the dips could be deeper. In those cases, the colour of the occulted system should eventually be dominated by the colour of the fainter object. However, our analysis in Section 3.4 has shown that there is no indication that the dimming is caused by anything other than interstellar dust grains of homogeneous scattering properties. In particular, for deep dips there is no deviation in the changes of colour from the prediction of extinction from dust. Thus, it seems highly unlikely that if there is a wide companion it is contributing a sizeable fraction of the system luminosity. Any closer companion would most likely disturb or remove the sub-au material in the accretion disc that we see in the system. Thus, V1490 Cyg is most likely single.

4.3 Literature NIR and MIR data for V1490 Cyg

In order to classify the evolutionary stage of the source, we have collected literature near- and mid-infrared photometry of the source. These data are summarized in Table 2. We have extracted the NIR photometry and observing dates from 2MASS (Skrutskie et al. 2006), UGPS (Lucas et al. 2008) data release DR11, and the MIR observations from NEOWISE (Mainzer et al. 2011, 2014) in the *W1* and *W2* bands from the *WISE* satellite (Wright et al. 2010). For the latter, we have averaged all the measurements taken over the usually 1–3 d repeated visits for the source and used the RMS as the uncertainty. The individual NEOWISE visits are too short to observe any changes related to the dipping behaviour. For completeness, we have further added *WISE* photometry released from the *WISE* all-sky catalogue (Cutri & et al. 2012) and the ALLWISE catalogue (Cutri & et al. 2013), as well as the *Spitzer* IRAC and MIPS photometry presented in Guieu et al. (2009) and Rebull et al. (2011).

As V1490 Cyg is variable, only data with a known observing date should be used for classification purposes (top part of the table). This is particularly important for the shorter wavelength data where the extinction is higher. Since we do not know how high the extinction was during past dipping events (if we do not have contemporary optical data), we should only use photometry taken during the phase of the light curve where the object is most likely at its maximum brightness. Considering the folded light curves in Figs. C1 and C2 in the online supplementary material and the period of $31.447 \pm 0.011 \text{ d}$ determined in Section 3.1, we have estimated the phase and its uncertainty for all NIR and MIR data with known observing dates. The star is considered to be in its bright state if the phase is within 0.15 of zero/one. These measurements are highlighted in Table 2 in bold face.

4.4 Evolutionary stage of V1490 Cyg

In order to estimate the evolutionary status of the source, we need to estimate the NIR and MIR magnitudes, not influenced by the variable circumstellar extinction. As is evident from Table 2, none of the available NIR data have been taken near the nominal bright state of the source. The variations of the four potential observations near the maximum brightness in *W1/W2* are of the order of several tenths of magnitudes. As evident in the folded light curves in Figs. C1 and C2 in the online supplementary material, the source can

Table 2. Summary of literature NIR/MIR data for V1490 Cyg. We list the Julian date of the observations, the filter/band the observations are in, the magnitude and uncertainty, the survey the data are taken from, and the phase and its uncertainty for the observation. The top part of the table lists data with available observing date, while in the bottom half time-averaged *WISE* and *Spitzer* photometry is listed for completeness. The NEOWISE data are averaged over the 1–3 d for each sequence of visits. The phase has been determined following the period determined in Section 3.1. The uncertainty in the phase has been propagated from the nominal 15 min uncertainty in the period. All magnitudes measured within 0.15 of phase zero are highlighted in bold, to indicate measurements that are most likely less influenced by the unknown variable circumstellar extinction.

Date (JD)	Filter	mag	Δ mag	Survey	Phase	Δ Phase
245 1707.8263	<i>J</i>	11.850	0.023	2MASS	0.206	0.078
245 1707.8263	<i>H</i>	11.008	0.032	2MASS	0.206	0.078
245 1707.8263	<i>K</i>	10.637	0.026	2MASS	0.206	0.078
245 7589.9499	<i>J</i>	12.0472	0.0006	UGPS	0.256	0.013
245 7589.9555	<i>H</i>	11.0429	0.0004	UGPS	0.256	0.013
245 7589.9597	<i>K</i>	10.7314	0.0006	UGPS	0.256	0.013
245 5861.7314	<i>K</i>	10.8222	0.0006	UGPS	0.299	0.032
245 6809.4858	<i>W1</i>	9.9188	0.0622	NEOWISE	0.437	0.021
245 6809.4858	<i>W2</i>	9.4490	0.0258	NEOWISE	0.437	0.021
245 6987.9896	<i>W1</i>	10.225	0.118	NEOWISE	0.113	0.019
245 6987.9896	<i>W2</i>	9.6490	0.0705	NEOWISE	0.113	0.019
245 7171.2939	<i>W1</i>	10.057	0.03	NEOWISE	0.942	0.017
245 7171.2939	<i>W2</i>	9.5810	0.0243	NEOWISE	0.942	0.017
245 7346.0040	<i>W1</i>	10.061	0.015	NEOWISE	0.498	0.015
245 7346.0040	<i>W2</i>	9.5360	0.0346	NEOWISE	0.498	0.015
245 7349.4515	<i>W1</i>	10.006	0.022	NEOWISE	0.608	0.015
245 7349.4515	<i>W2</i>	9.5000	0.0182	NEOWISE	0.608	0.015
245 7535.4401	<i>W1</i>	10.191	0.057	NEOWISE	0.522	0.013
245 7535.4401	<i>W2</i>	9.6460	0.0279	NEOWISE	0.522	0.013
245 7538.7336	<i>W1</i>	10.040	0.032	NEOWISE	0.627	0.013
245 7538.7336	<i>W2</i>	9.4930	0.0171	NEOWISE	0.627	0.013
245 7708.6578	<i>W1</i>	9.9273	0.0701	NEOWISE	0.030	0.011
245 7708.6578	<i>W2</i>	9.4918	0.0551	NEOWISE	0.030	0.011
245 7902.4970	<i>W1</i>	9.9078	0.0227	NEOWISE	0.194	0.009
245 7902.4970	<i>W2</i>	9.4613	0.0146	NEOWISE	0.194	0.009
245 8069.3243	<i>W1</i>	9.9929	0.0441	NEOWISE	0.500	0.007
245 8069.3243	<i>W2</i>	9.4577	0.0568	NEOWISE	0.500	0.007
245 8266.6522	<i>W1</i>	9.8730	0.0221	NEOWISE	0.774	0.005
245 8266.6522	<i>W2</i>	9.3924	0.0196	NEOWISE	0.774	0.005
245 8429.9023	<i>W1</i>	9.8158	0.0257	NEOWISE	0.966	0.003
245 8429.9023	<i>W2</i>	9.3902	0.0408	NEOWISE	0.966	0.003
–	<i>W1</i>	9.929	0.023	<i>WISE</i> all sky	–	–
–	<i>W2</i>	9.412	0.021	<i>WISE</i> all sky	–	–
–	<i>W3</i>	7.300	0.028	<i>WISE</i> all sky	–	–
–	<i>W4</i>	5.209	0.036	<i>WISE</i> all sky	–	–
–	<i>W1</i>	9.937	0.023	AllWISE	–	–
–	<i>W2</i>	9.443	0.021	AllWISE	–	–
–	<i>W3</i>	7.427	0.029	AllWISE	–	–
–	<i>W4</i>	5.163	0.037	AllWISE	–	–
–	3.6	9.956	–	IRAC	–	–
–	4.5	9.581	–	IRAC	–	–
–	5.8	9.036	–	IRAC	–	–
–	8.0	8.211	–	IRAC	–	–
–	24	5.387	–	MIPS	–	–

vary quite significantly even close to the nominally bright phase. Hence, we will use the brightest of the *JHK/W1/W2* magnitudes for the classification, but note that the resulting colours are potentially uncertain by a few tenths of a magnitude. Similarly, we choose the brightest of the *W3/W4* measurements from the *WISE* all-sky and ALLWISE catalogues.

Table 3. Observation dates of LCOGT optical spectra and the measured $H\alpha$ equivalent width for V1490 Cyg. The uncertainties in the equivalent widths are about 0.3 Å.

Julian date	EW (Å)
245 8338.7817	–4.31
245 8343.9943	–5.30
245 8348.8409	–4.36
245 8368.9099	–8.63
245 8373.8684	–3.29
245 8376.9494	–3.49

Thus, we find $H-K = 0.37$ mag, $W1-W2 = 0.43$ mag, and $W3-W4 = 2.1$ mag. According to Koenig & Leisawitz (2014), this places the source at the blue end of the classification as a CTTS in the $W1-W2$ versus $H-K$ diagram, or just outside, considering the potential uncertainties in the colours. In the $W3-W4$ versus $W1-W2$ diagram, the source sits on the border line between CTTS and transition disc objects. Using the *WISE* data and following Majaess (2013), we determine the slope (α_{SED}) of the spectral energy distribution as -0.67 . This places the source in the CTTS category.

Our spectra from LCOGT (see Section 2.4) allow us to use the $H\alpha$ EW to classify the source. In the six spectra obtained the EW of the $H\alpha$ line varies between -3.2 and -8.6 Å. The most widely used dividing line between CTTS and WTTS is -10 Å (e.g. Martín 1998). However, this is not a fixed value due to the variability of the line.

The source is, however, still accreting and all available accretion rate indicators show variability. The $H\alpha$ EW (see Fig. 4 and Table 3) is clearly variable by at least a factor of 2. Furthermore, the $R_c-H\alpha$ magnitudes also vary by at least 1 mag, i.e. more than a factor of 2. Finally, as can be seen in Fig. 6, the *U* band is highly variable by at least ± 2 mag even on very short (hours) time-scales. Since the *U*-band excess is generally acknowledged as one of the best tracers of accretion rate, both empirically (Gullbring et al. 1998; Herczeg & Hillenbrand 2008) and theoretically (Calvet & Gullbring 1998), this indicates strongly variable accretion in V1490 Cyg.

Thus, we conclude that V1490 Cyg is most likely a CTTS, with (currently) a low, but variable accretion rate, and is potentially at the start of the transition into a WTTS or transition disc object.

4.5 The nature of V1490 Cyg

Our analysis presented in Sections 3.1–4.4 shows that V1490 Cyg is showing quasi-periodic occultation events of dust in the inner accretion disc at 0.15 au from the source. The occulting material is made of material with ISM properties at low A_V and shows grain growth at high column densities. The source is still accreting and is at the borderline between CTTS/WTTS or transition disc objects. Below we briefly discuss three possible explanations for the nature of the source, in order of decreasing probability: (i) a protoplanet-induced disc warp; (ii) a magnetically induced disc warp; (iii) the Hill sphere of an accreting protoplanet. Attempting to verify these explanations will require high-resolution spectroscopy over several orbital periods, which we strongly encourage.

4.5.1 Protoplanet-induced disc warp

Recent Atacama Large Millimeter/sub-millimeter Array (ALMA) observations have discovered several warped protostellar disc systems (Sakai et al. 2019). For some of these systems, observations rule out the influence of a secondary star, potentially suggesting un-

seen protoplanets to be the cause of the warping (Nealon et al. 2018). A protoplanet that is capable of driving warping features in the disc would be required to maintain an orbit that is inclined to the disc plane over long time-scales. This is, however, in contradiction with current planet formation theory that assumes a flat protoplanetary disc. A co-planar protoplanet could become inclined or eccentric during or after formation, whereby planet–planet interactions are able to move a protoplanet to an inclined orbit (Nagasawa, Ida & Bessho 2008). Measurements of disc inclination in objects such as TW Hya hint at a small warp or misalignment, at distances less than 1 au for even minor deviations in inclination from the disc plane (Qi et al. 2004; Pontoppidan et al. 2008; Hughes et al. 2011). The azimuthal surface brightness asymmetry moving with a constant angular velocity in TW Hya has also been attributed to a planet-induced warp in the inner disc of that system (Debes et al. 2017). Simulations by, e.g. Nealon et al. (2019) show that misaligned planetary orbits are indeed capable of generating such warps.

In Section 3.4, we have shown that the material in the occulting structure appears to consist of low-column density material, with roughly ISM dust properties. Embedded in this envelope are denser, small-scale structures that are most likely composed of larger dust grains. This, combined with the fact that the source is situated in an ~ 3 Myr star-forming region (Bally et al. 2008), suggests that planet formation should be ongoing. The source exhibits dips across the majority of the observed periods, demonstrating semistability in the occulting structure. Orbital resonance between the disc and an inclined orbiting protoplanet could cause a build-up of material at the distances observed. Such a protoplanet could be closer to, or further from the source in relation to the observed orbiting structure.

4.5.2 Magnetically induced disc warp

The observed regular dips of V1490 Cyg suggest that it could be an AA Tau-type source. However, the period of 31.447 d is particularly long compared to other AA Tau-type objects. Average rotational periods of CTTs are 7.3 d (Bouvier et al. 1995), with AA Tau itself having a period of 8.2 d (Bouvier et al. 2003). Hence, typical values range between 5 and 10 d.

In AA Tau-type objects, the periodic dips are caused by a warp of the inner disc due to a misalignment between the rotation axes of both the disc and the star. The warp is therefore located at the co-rotation radius of the disc (Bouvier et al. 1999, 2007; Cody et al. 2014; McGinnis et al. 2015). Assuming a dipole magnetic field aligned with the star’s rotation axis, material in the disc would be magnetically displaced from the disc’s plane and into the line of sight. If V1490 Cyg is seen at a high inclination, the inner disc warp will occult the stellar photosphere periodically, causing flux dips in the star’s light curve. This obscuration could then explain such dimming behaviour as seen in Section 3.1. However, for V1490 Cyg to have a warped disc due to misalignment, the source would have to be a very slow rotator. This would enable the co-rotation radius, and hence the disc warp, to occur further out than is seen for AA Tau. Note that 30 d or slower rotation periods in young clusters are extremely rare (see e.g. Bouvier et al. 2014), and that the magnetic field would have to be very strong and reach far out from the star to generate a warp at the observed distance of 0.15 au.

4.5.3 Hill sphere of accreting protoplanet

It is also conceivable that the observed quasi-periodic variability observed in V1490 Cyg comes from material held in orbit not by

a magnetic structure, but by a more massive object. A protoplanet located at distances close to the central star within the disc will gravitationally exert influence on the disc material around it. The occultations observed could then be caused by material in the Hill sphere around this protoplanet. The Hill sphere presents as an oblate spheroid of material, gravitationally bound to the protoplanet within the disc. Modelling by Papaloizou & Nelson (2005) suggests that for a protoplanetary mass of $\sim 0.1 M_J$, a rapid accretion phase begins. This is a similar mass to that for which either significant perturbation to the protoplanetary disc through local mass accretion or disc–planet interaction begins (Nelson et al. 2000).

On its own, structures of the mass observed in Section 3.3 will not survive for more than one orbit due to shearing. The periodic dips in V1490 Cyg are stable in phase, if not in structure, for more than 40 orbits. We do consider this explanation as the least likely, since the duration of dips observed for the source span more than half the period in many cases and the deepest part of the occultations move significantly in phase. This is not in good agreement with predictions for this scenario as the size of the Hill sphere will not exceed 0.1–0.2 of the orbital circumference, i.e. the maximum duration of the dips should be no longer than approximately 6 d.

5 CONCLUSIONS

In this work, we present results from our long-term, high-cadence, multifilter optical monitoring of young, nearby star clusters and star-forming regions obtained as part of the HOYS programme (Froeblich et al. 2018b). The data set consists of images taken with a wide variety of telescopes, detectors, and filters, with images also obtained under a variety of observing (light pollution) and weather conditions (from photometric to thin or even thick cirrus). The availability of a large amount of images (~ 3300) obtained over a long period (~ 4 yr) has enabled us to develop an internal photometric calibration procedure to remove systematic magnitude offsets due to colour terms in the photometry. This utilizes non-variable sources that are identifiable in the data. The procedure achieves for the star V1490 Cyg ($V \approx 15.5$ mag) a median uncertainty in the photometry of 0.02 mag in all broad-band filters (U , B , V , R_c , and I_c) and 0.09 mag in $H\alpha$.

Our analysis of the Orion variable V1490 Cyg in the Pelican Nebula (IC 5070) shows that it is actually a quasi-periodic dipper, most likely caused by occultations of the star by material in a warped inner disc. A mean period of 31.447 ± 0.011 d was determined in the V , R_c , and I_c filters using a Lomb–Scargle periodogram. This variability is quasi-periodic, with varying depth from orbit to orbit. However, the period is stable over the 4 yr of continuous observations available from HOYS. The B , V , R_c , and I_c light curves follow an extremely similar pattern on all time-scales, caused by the variations in the column density along the line of sight. However, the U and $R_c - H\alpha$ data do not follow the same variations and in part show more extreme variation on time-scales of hours to days. This suggests that the variability in those accretion rate indicators is indeed dominated by changes in the mass accretion rate in the system. The U -band data in particular show variability of up to a factor of 10 on time-scales of hours.

We investigate the behaviour of the source in the V versus $V - I_c$ parameter space. We find that the material in the occulting structure consists in part of low-column density material (A_V), with roughly ISM dust properties (R_V). Embedded in this envelope are denser, higher column density, small-scale structures that are most likely composed of dust grains that are larger than in the ISM. The scattering properties of this material are consistent and do not

change over time, indicating a mixing of material in the disc before it is moved into the observable structure.

An analysis of the column density distribution of consecutive dips, i.e. the structure function of the material, has been performed. We find no significant or systematic trends in the structure function. This suggests that the material in the line of sight is moving in and out of the occulting structure on time-scales of the order of, or shorter than the period of the occultations (~ 30 d). We determine the amount of mass in the occulting structure for each orbit and find it to vary by up to a factor of 10 for both mass increase and decrease. Thus, the mass flow rate through the occulting structure varies by typically a factor of a few when averaged over one period. This converts to a minimum mass accretion rate through the occulting structure on to V1490 Cyg of the order of $10^{-10} M_{\odot} \text{ yr}^{-1}$. This is consistent with low levels of accretion as seen in other T Tauri stars.

The *Gaia* DR2 parallax of V1490 Cyg is highly uncertain, most likely due to the variability and red colour. We hence use *Gaia* DR2 data from the stars in the same field to determine an accurate distance to IC 5070. We find a distance of 870^{+70}_{-55} pc for the Pelican Nebula.

The NIR and MIR data taken from literature, our measured $H\alpha$ equivalent widths, and the U -band and $R_c-H\alpha$ variability indicate that V1490 Cyg is most likely a CTTS, with a currently low, but variable accretion rate, that is potentially at the start of the transition into a WTTS or transition disc object.

Our data and analysis show that V1490 Cyg seems to have a warped inner accretion disc, which enables us to observe the structure periodically. Assuming that the central star is about half a solar mass, this places the orbiting material at a distance of ~ 0.15 au from the central star. The most likely interpretation for the cause of the warp is a protoplanetary object with an inclined orbit, located somewhere in the inner accretion disc. There is also the possibility that the warp is magnetically induced similar to an AA Tau-like object. However, this would require V1490 Cyg to be a very slow rotator. Finally, we also study the possibility that the orbiting structures are associated with the Hill sphere of an accreting protoplanet. However, the long duration of the observed occultations seems to refute this explanation. Longer term high-resolution spectroscopy of the object is encouraged to identify the true nature of V1490 Cyg.

ACKNOWLEDGEMENTS

We would like to thank all contributors of data (even if they decided not to have their name on the author list of the paper) for their efforts towards the success of the HOYS project. We thank Nigel Hambly for advice on interpreting *Gaia* data uncertainties. JJE acknowledges a joint University of Kent and STFC scholarship (ST/S505456/1). AS acknowledges support through STFC grant ST/R000824/1. JC-W acknowledges the studentship provided by the University of Kent. SVM acknowledges an STFC scholarship (1482158). KW thanks Ray McErlean and Dipali Thanki for technical support of the UL50 operations. KW acknowledges funding by STFC. KW acknowledges support from Royal Society Research Grant RG170230 (PI: R. Starling). DM acknowledges the support from NCN grant 2016/21/B/ST9/01126. TK thanks the OpenScience Observatories team at the Open University for allowing the use of and operating the COAST facility. This work makes use of observations from the LCOGT network. This work was supported by the Slovak Research and Development Agency

under the contract no. APVV-15-0458. This publication makes use of data products from the Near-Earth Object Wide-field Infrared Survey Explorer (NEOWISE), which is a project of the Jet Propulsion Laboratory/California Institute of Technology. NEOWISE is funded by the National Aeronautics and Space Administration. This research has made use of the SIMBAD data base, operated at CDS, Strasbourg, France. We acknowledge the use of the Cambridge Photometric Calibration Server (<http://gsaweb.ast.cam.ac.uk/followup>), developed and maintained by Lukasz Wyrzykowski, Sergey Koposov, Arancha Delgado, and Pawel Zielinski, and funded by the European Union's Horizon 2020 research and innovation programme under grant agreement no. 730890 (OPTICON).

REFERENCES

- Alcalá J. M. et al., 2017, *A&A*, 600, A20
 Andrews S. M. et al., 2018, *ApJ*, 869, L41
 Ansdell M. et al., 2016, *ApJ*, 816, 69
 Auvergne M. et al., 2009, *A&A*, 506, 411
 Avenhaus H. et al., 2018, *ApJ*, 863, 44
 Bacher A., Kimeswenger S., Teutsch P., 2005, *MNRAS*, 362, 542
 Bally J., Walawender J., Johnstone D., Kirk H., Goodman A., 2008, in Reipurth B., The Perseus Cloud. The Northern Sky ASP Monograph Publications, p. 308
 Bertin E., Arnouts S., 1996, *A&AS*, 117, 393
 Bouvier J., Covino E., Kovo O., Martin E. L., Matthews J. M., Terranegra L., Beck S. C., 1995, *A&A*, 299, 89
 Bouvier J. et al., 1999, *A&A*, 349, 619
 Bouvier J. et al., 2003, *A&A*, 409, 169
 Bouvier J. et al., 2007, *A&A*, 463, 1017
 Bouvier J., Matt S. P., Mohanty S., Scholz A., Stassun K. G., Zanni C., 2014, in Beuther H., Klessen R. S., Dullemond C. P., Henning T., eds, Protostars and Planets VI. Univ. Arizona Press, Tucson, p. 433
 Bozhinova I. et al., 2016, *MNRAS*, 463, 4459
 Calvet N., Gullbring E., 1998, *ApJ*, 509, 802
 Carpenter J. M., Hillenbrand L. A., Skrutskie M. F., 2001, *AJ*, 121, 3160
 Cody A. M. et al., 2014, *AJ*, 147, 82
 Contreras Peña C. et al., 2014, *MNRAS*, 439, 1829
 Contreras Peña C. et al., 2017, *MNRAS*, 465, 3011
 Contreras Peña C., Naylor T., Morrell S., 2019, *MNRAS*, 486, 4590
 Cutri R. M. et al., 2012, VizieR Online Data Catalog, p. II/311
 Cutri R. M. et al., 2013, VizieR Online Data Catalog, p. II/328
 Debes J. H. et al., 2017, *ApJ*, 835, 205
 Findeisen K., Hillenbrand L., Ofek E., Levitan D., Sesar B., Laher R., Surace J., 2013, *ApJ*, 768, 93
 Findeisen K., Cody A. M., Hillenbrand L., 2015, *ApJ*, 798, 89
 Froebrich D. et al., 2018a, *Res. Notes Am. Astron. Soc.*, 2, 61
 Froebrich D. et al., 2018b, *MNRAS*, 478, 5091
 Gaia Collaboration, 2018, VizieR Online Data Catalog, p. I/345
 Guieu S. et al., 2009, *ApJ*, 697, 787
 Gullbring E., Hartmann L., Briceño C., Calvet N., 1998, *ApJ*, 492, 323
 Herbst W., Shevchenko V. S., 1999, *AJ*, 118, 1043
 Herczeg G. J., Hillenbrand L. A., 2008, *ApJ*, 681, 594
 Hogg D. W., Blanton M., Lang D., Mierle K., Roweis S., 2008, in Argyle R. W., Bunclark P. S., Lewis J. R., eds, ASP Conf. Ser. Vol. 394, Astronomical Data Analysis Software and Systems XVII. Astron. Soc. Pac., San Francisco, p. 27
 Hughes A. M., Wilner D. J., Andrews S. M., Qi C., Hogerheijde M. R., 2011, *ApJ*, 727, 85
 Ibraymov S., Semkov E., Milanov T., Peneva S., 2018, *Res. Astron. Astrophys.*, 18, 137
 Joy A. H., 1945, *ApJ*, 102, 168
 Koenig X. P., Leisawitz D. T., 2014, *ApJ*, 791, 131
 Leung H. W., Bovy J., 2019, *MNRAS*, 489, 2079

Lucas P. W. et al., 2008, *MNRAS*, 391, 136
 McGinnis P. T. et al., 2015, *A&A*, 577, A11
 Mainzer A. et al., 2011, *ApJ*, 731, 53
 Mainzer A. et al., 2014, *ApJ*, 792, 30
 Majaess D., 2013, *Ap&SS*, 344, 175
 Martin E. L., 1998, *AJ*, 115, 351
 Mathis J. S., 1990, *ARA&A*, 28, 37
 Matsakos T. et al., 2013, *A&A*, 557, A69
 Moffat A. F. J., 1969, *A&A*, 3, 455
 Nagasawa M., Ida S., Bessho T., 2008, *ApJ*, 678, 498
 Nealon R., Dipierro G., Alexander R., Martin R. G., Nixon C., 2018, *MNRAS*, 481, 20
 Nealon R., Pinte C., Alexander R., Mentiplay D., Dipierro G., 2019, *MNRAS*, 484, 4951
 Nelson R. P., Papaloizou J. C. B., Masset F., Kley W., 2000, *MNRAS*, 318, 18
 Ogura K., Sugitani K., Pickles A., 2002, *AJ*, 123, 2597
 Papaloizou J. C. B., Nelson R. P., 2005, *A&A*, 433, 247
 Pontoppidan K. M., Blake G. A., van Dishoeck E. F., Smette A., Ireland M. J., Brown J., 2008, *ApJ*, 684, 1323
 Qi C. et al., 2004, *ApJ*, 616, L11
 Rebull L. M. et al., 2011, *ApJS*, 193, 25
 Reipurth B., Schneider N., 2008, in Reipurth B., ed., *Star Formation and Young Clusters in Cygnus*. The Northern Sky ASP Monograph Publications, p. 36
 Ricker G. R. et al., 2015, *J. Astron. Telesc. Instrum. Syst.*, 1, 014003
 Rigon L., Scholz A., Anderson D., West R., 2017, *MNRAS*, 465, 3889
 Sacco G. G., Argiroffi C., Orlando S., Maggio A., Peres G., Reale F., 2008, *A&A*, 491, L17
 Sakai N., Hanawa T., Zhang Y., Higuchi A. E., Ohashi S., Oya Y., Yamamoto S., 2019, *Nature*, 565, 206
 Samus' N. N. et al., 2003, *Astron. Lett.*, 29, 468
 Sand D., 2014, in Wozniak P. R., Graham M. J., Mahabal A. A., Seaman R., eds, *The Third Hot-Wiring the Transient Universe Workshop*. p. 187
 Scargle J. D., 1982, *ApJ*, 263, 835
 Scholz A., Eisloffel J., 2004, *A&A*, 419, 249
 Skrutskie M. F. et al., 2006, *AJ*, 131, 1163
 Welch D. L., Stetson P. B., 1993, *AJ*, 105, 1813
 Wright E. L. et al., 2010, *AJ*, 140, 1868

SUPPORTING INFORMATION

Supplementary data are available at *MNRAS* online.

APPENDIX A: Description of observatories and data reduction.

APPENDIX B: Long-term light curves of V1490 Cyg.

APPENDIX C: Lomb-scargle periodograms.

APPENDIX D: *Gaia* parallax versus proper motion in IC 5070 V1490 Cyg.

Please note: Oxford University Press is not responsible for the content or functionality of any supporting materials supplied by

the authors. Any queries (other than missing material) should be directed to the corresponding author for the article.

¹*Centre for Astrophysics and Planetary Science, School of Physical Sciences, University of Kent, Canterbury CT2 7NH, UK*

²*SUPA, School of Physics and Astronomy, University of St Andrews, North Haugh, St Andrews KY16 9SS, UK*

³*Thüringer Landessternwarte, Sternwarte 5, D-07778 Tautenburg, Germany*

⁴*SUPA, School of Science and Engineering, University of Dundee, Nethergate, Dundee DD1 4HN, UK*

⁵*School of Computing, University of Kent, Canterbury CT2 7NF, UK*

⁶*The British Astronomical Association, Variable Star Section, Burlington House Piccadilly, London W1J 0DU, UK*

⁷*Department of Physics, University of Warwick, Coventry CV4 7AL, UK*

⁸*University of Leicester, University Road, Leicester LE1 7RH, UK*

⁹*Vihorlat Observatory, Mierová 4, 06601 Humenné, Slovakia*

¹⁰*Observadores de Supernovas, Spain*

¹¹*AAVSO, 49 Bay State Road, Cambridge, MA 02138, USA*

¹²*Asociacion Astronomica Cruz del Norte, Calle Caceres 18, E-28100 Alcobendas, Madrid, Spain*

¹³*Center for Backyard Astrophysics Extremadura, E-06340 Fregenal de la Sierra, Spain*

¹⁴*Vereniging voor Sterrenkunde VVS, B-3401 Landen, Belgium*

¹⁵*Sociedad Astronómica Asturiana 'Omega', Spain*

¹⁶*School of Physical Sciences, The Open University, Walton Hall, Milton Keynes MK7 6AA, UK*

¹⁷*Center for Backyard Astrophysics, Piazzetta del Gesù 3, I-73034 Gagliano del Capo, Italy*

¹⁸*Agrupacio Astronomica de Sabadell, C/ Prat de la Riba s/n, E-08206 Sabadell (Barcelona), Spain*

¹⁹*Hampshire Astronomical Group, Clanfield, UK*

²⁰*Instytut Astronomiczny, Uniwersytet Wrocławski, Kopernika 11, PL-51-622 Wrocław, Poland*

²¹*Astronomical Society of Edinburgh, Edinburgh, UK*

²²*Wiltshire Astronomical Society, 2 Oathills, Corsham SN13 9NL, UK*

²³*The William Herschel Society, The Herschel Museum of Astronomy, 19 New King Street, Bath BA1 2BL, UK*

²⁴*Public Observatory AstroLAB IRIS, Provinciaal Domein De Palingbeek, Verbrandemolenstraat 5, B-8902 Zillebeke, Ieper, Belgium*

²⁵*Vereniging voor Sterrenkunde, Werkgroep Veranderlijke Sterren, Oostmeers 122 C, B-8000 Brugge, Belgium*

²⁶*Center for Mathematical Plasma Astrophysics, University of Leuven, Oude Markt 13, 3000 Leuven, Belgium*

²⁷*San Diego Astronomy Association, PO Box 23215, San Diego, CA 92193-321, US*

²⁸*Tigra Astronomy, 16 Laxton Way, Canterbury, Kent CT1 1FT, UK*

²⁹*Sociedad Malagueña de Astronomía (SMA), Málaga, Spain*

³⁰*Selztal Observatory, D-55278 Friesenheim, Bechtolsheimer Weg 26, Germany*

This paper has been typeset from a \LaTeX file prepared by the author.